

See discussions, stats, and author profiles for this publication at: <https://www.researchgate.net/publication/263584217>

Light-Emitting Diodes Based on Solution-Processed Nontoxic Quantum Dots: Oxides as Carrier-Transport Layers and Introducing Molybdenum Oxide Nanoparticles as a Hole-Inject Layer

ARTICLE in ACS APPLIED MATERIALS & INTERFACES · JULY 2014

Impact Factor: 6.72 · DOI: 10.1021/am501890m · Source: PubMed

CITATIONS

2

READS

142

2 AUTHORS:



Saikat Bhaumik

Indian Association for the Cultivation of Science

8 PUBLICATIONS 46 CITATIONS

SEE PROFILE



Jay Prakash Pal

Uttar Pradesh Technical University

99 PUBLICATIONS 1,196 CITATIONS

SEE PROFILE

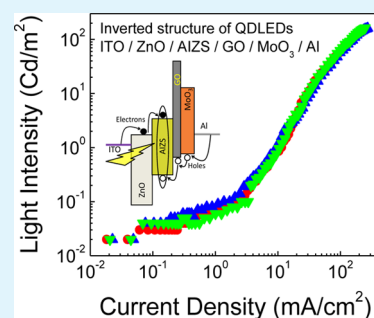
Light-Emitting Diodes Based on Solution-Processed Nontoxic Quantum Dots: Oxides as Carrier-Transport Layers and Introducing Molybdenum Oxide Nanoparticles as a Hole-Inject Layer

Saikat Bhaumik and Amlan J. Pal*

Department of Solid State Physics, Indian Association for the Cultivation of Science, Jadavpur, Kolkata 700032, India

ABSTRACT: We report fabrication and characterization of solution-processed quantum dot light-emitting diodes (QDLEDs) based on a layer of nontoxic and Earth-abundant zinc-diffused silver indium disulfide (AIZS) nanoparticles as an emitting material. In the QDLEDs fabricated on indium tin oxide (ITO)-coated glass substrates, we use layers of oxides, such as graphene oxide (GO) and zinc oxide (ZnO) nanoparticles as a hole- and electron-transport layer, respectively. In addition, we introduce a layer of MoO_3 nanoparticles as a hole-inject one. We report a comparison of the characteristics of different device architectures. We show that an inverted device architecture, ITO/ZnO/AIZS/GO/ MoO_3 /Al, yields a higher electroluminescence (EL) emission, compared to direct ones, for three reasons: (1) the GO/ MoO_3 layers introduce barriers for electrons to reach the Al electrode, and, similarly, the ZnO layers acts as a barrier for holes to travel to the ITO electrode; (2) the introduction of a layer of MoO_3 nanoparticles as a hole-inject layer reduces the barrier height for holes and thereby balances charge injection in the inverted structure; and (3) the wide-bandgap zinc oxide next to the ITO electrode does not absorb the EL emission during its exit from the device. In the QDLEDs with oxides as carrier inject and transport layers, the EL spectrum resembles the photoluminescence emission of the emitting material (AIZS), implying that excitons are formed in the quaternary nanocrystals and decay radiatively.

KEYWORDS: quantum dot light-emitting diodes, inverted structure, zinc-diffused silver indium disulfide, graphene oxide, oxides as charge-inject and transport layers, MoO_3 nanoparticles



INTRODUCTION

With the genesis of quantum dot light-emitting diodes (QDLEDs) being organic light-emitting diodes (OLEDs), researchers over the years have intended to introduce a range of novel materials in their lower-dimensional form in the diodes.^{1–10} It may be recalled that the device structure generally involves hole- and electron-inject and transport layers apart from an emitting layer in which excitons form and finally decay radiatively to yield electroluminescence (EL) emission. Efforts have hence been made to select materials in each of the layers in order to optimize their functions in the QDLEDs. To do so, a range of issues are being considered, such as processability of the nanomaterials,^{10,11} stability of the devices,^{7,12,13} (non)toxicity of the elements used in the materials,^{2,9,14–16} and so on.

In the quest of nanomaterials for QDLEDs, doped binary systems, such as ZnS with copper and manganese ions as dopants,^{4,5} have been a novel route. In the doped semiconductors, photoluminescence (PL) emission of the nanomaterials and hence EL of devices based on such nanostructures involve the *d*-states of the dopants.^{17,18} Researchers have also considered ternary and quaternary systems as a route to avoid toxic elements, zinc-diffused copper indium disulfide (CIZS) and silver indium disulfide (AIZS) being some such examples.^{14–16} The QDLEDs based on quantum dots containing nontoxic elements were initially formed with other

conventional polymer/organic layers restricting the stability of hybrid or QDLEDs.

At this point, researchers turned to oxides having suitable hole- and electron-injection and transport abilities and a higher device stability.^{12,13,19–22} The materials in this regard were nickel oxide,^{22,23} intrinsic and doped zinc oxide,^{12,13,21–23} tungsten oxide,¹³ tin oxide,¹⁹ molybdenum oxide,^{7,20,24} titanium dioxide,²⁵ graphene oxides,^{26,27} etc. While nanoparticles of nickel, tungsten, and graphene oxides have been used in the form of a hole-transport layer, thin films of zinc, tin, and titanium oxides were used as an electron-inject layer. Recently, thin films of MoO_3 grown via either a high-temperature sputtering technique or a sol–gel technique have been used as a hole-transport layer in QDLEDs.^{7,20,24} In this work, we introduce nanoparticles of molybdenum oxide (MoO_3), grown via a colloidal synthetic method, as a carrier-inject material. Such nanoparticles have so far been used in solar cells for efficient hole-transport and extraction process.^{28,29}

The other aspects that we kept in mind in designing the QDLEDs are the bandgap of the carrier-transport layers. It is important that the material that lies between the emitting layer and the semitransparent electrode (indium tin oxide, ITO) must not absorb the EL emission that exits directly through the

Received: March 28, 2014

Accepted: July 1, 2014

Published: July 1, 2014



ITO electrode. It is therefore required that a high bandgap material is placed next to the semitransparent electrode, irrespective of the type of carriers the high bandgap material would transport. Since MoO_3 has a lower bandgap, compared to other oxides, a layer of it on the ITO electrode acting as a hole-inject electrode of a conventional device-architecture was not encouraging, since the MoO_3 layer would absorb the EL emission before its exit through the semitransparent electrode. This has enforced formation of an inverted structure with the ITO being an electron-inject one.^{7,19,21,30,31} Such an inverted geometry has been found to balance charge injection and enhance device stability.⁷ We hence aimed to put ZnO near the ITO and a layer of MoO_3 nanoparticles near the opaque one (aluminum). In such an inverted device-architecture, while the MoO_3 would assist hole-injection in the devices to obtain a balance in injected charges, the ZnO and GO would block flow of holes and electrons, respectively, to the electrodes, so that formation of excitons in the emitting layer is enforced or encouraged. With AIZS nanoparticles as the emitting material and graphene oxide (GO) as hole-transport layer, the ITO/ZnO/AIZS/GO/ MoO_3 /Al devices hence act as solution-processed QLEDs based on nontoxic elements with all-oxide charge inject and transport materials.

EXPERIMENTAL SECTION

Materials. Indium(III) acetate, $\text{In}(\text{OAc})_3$, zinc(II) acetate, $\text{Zn}(\text{OAc})_2$, zinc(II) acetate dihydrate, $\text{Zn}(\text{OAc})_2 \cdot 2\text{H}_2\text{O}$, silver(I) acetate, $\text{Ag}(\text{OAc})$, zinc(II) stearate, tetramethylammonium hydroxide (TMAH, 25 wt % in methanol), triethylphosphine (TOP, 90%), sulfur powder (99.9%), 1-dodecanethiol (DDT), oleylamine (OAm), and 1-octadecene (ODE) were purchased from Aldrich Chemical Co. Graphite powder was purchased from Alfa Aesar. Ammonium molybdate tetrahydrate, $(\text{NH}_4)_6\text{Mo}_7\text{O}_{24} \cdot 4\text{H}_2\text{O}$ (AMT), dimethyl sulfoxide (DMSO), ethyl acetate, sodium nitrate, sulfuric acid (H_2SO_4), potassium permanganate (KMnO_4), and H_2O_2 were purchased from Merck. All the chemicals were used without further purification.

Preparation of Stock Solutions. To form a stock solution of sulfur, 9 mg of sulfur powder (0.3 mM) was mixed in 0.5 mL OAm and 1.5 mL ODE in a glass vial. After degassing the solvent for 15 min by purging ultrahigh pure nitrogen, the flask was heated to 100–120 °C to obtain the stock solution.

A stock solution of zinc and sulfur (1:1) was formed for the growth of a shell layer. To do so, 252 mg of zinc stearate (0.4 mM) and 12 mg of sulfur powder (0.4 mM) was mixed in 1 mL of TOP and 3 mL of ODE in a separate glass vial. After degassing for 15 min, the vial was heated to 100–120 °C to obtain a clear solution.

Synthesis of AIZS Nanoparticles. AIZS nanoparticles were grown by a reported colloidal synthetic method.^{16,32} In a typical synthesis, 8.4 mg of $\text{Ag}(\text{OAc})$ (0.05 mM), 29 mg of $\text{In}(\text{OAc})_3$ (0.1 mM), 18 mg of $\text{Zn}(\text{OAc})_2$ (0.1 mM), 2 mL of DDT, 0.2 mL of OAm, and 5 mL of ODE were mixed in a three-neck glass flask. At first, the reaction flask was degassed for 20 min under a vigorous stirring condition; the temperature of the contents was slowly raised to 100 °C. After 5 min, the temperature of the reaction flask was increased to 200 °C. At this stage, sulfur-stock solution (1.5 mL) was injected to the flask; reaction was allowed to continue for 5 min for the growth of AIZS nanoparticles. The temperature of the reaction flask was further raised to 230 °C before 1 mL of zinc and sulfur mixed stock-solution was injected. The reaction was allowed to continue for another 30 min to complete the formation of a shell layer of ZnS on AIZS nanoparticles that enhances the PL intensity. Here, zinc is also known to occupy the vacancies at the silver sites, thereby improving PL emission of the nanocrystals. The reaction was stopped by cooling the temperature of the flask down to room temperature. The as-prepared AIZS nanoparticles were purified by adding an excess

amount of acetone and ethanol as nonsolvents. The nanoparticles yielded yellow emission under ultraviolet (UV) irradiation.

Synthesis of ZnO Nanoparticles. ZnO nanoparticles were grown at room temperature following a reported route.³³ At first, 0.101 M zinc acetate dihydrate powder was dissolved in DMSO (30 mL) under a vigorous stirring condition at 50 °C. TMAH (0.552 M) dissolved in 10 mL of ethanol was added dropwise to zinc acetate solution at a rate of 2 mL/min to enable the formation of ZnO nanoparticles. After 5 min, 50 mL of ethyl acetate was added to the reaction mixture and the temperature of the reactant was cooled rapidly to stop the reaction process. The as-prepared ZnO nanoparticles were precipitated by centrifugation and redissolved in ethanol for further use.

Synthesis of Graphene Oxide. Graphene oxide was prepared using Hummer's method.³⁴ Graphite powder (100 mg) and sodium nitrate (50 mg) were added to concentrated H_2SO_4 (2.5 mL) and stirred for a day. The temperature of the mixed solution was lowered to 0 °C before adding KMnO_4 (300 mg) under a vigorous stirring condition. When KMnO_4 dissolved completely, the temperature of the solution was slowly raised to 35 ± 5 °C and maintained for 30 min. A brownish gray paste formed. Water (5 mL) was added slowly, followed by increasing the temperature of the reaction flask to 98 °C. A violent effervescence occurred, with the solution turning brownish yellow. The temperature of the reactants was maintained for 15 min. Warm water (14 mL) and 3% H_2O_2 (500 μL) were added in sequence to reduce the unreacted permanganate. The brownish light-yellow particles were centrifuged at 14,000 rpm for 30 min and washed thoroughly with warm water until neutralization. The solid was air-dried followed by vacuum-drying at 70 °C. The material was exfoliated in 50 mL deionized water under sonication for 15 min followed by centrifugation at 4000 rpm for 20 min. The supernatant was collected in distilled water as dispersed solution of GO.

Synthesis of Molybdenum Oxide Nanoparticles. Ammonium molybdate tetrahydrate (0.2 mmol) and oleylamine (20 mL) were mixed in a reaction flask. The contents were degassed thoroughly before raising the temperature to 100 °C that was maintained for 10 min. The temperature of the flask was then slowly increased to 250 °C. The reaction was allowed to continue for 3 h before cooling the flask down to room temperature. The MoO_3 nanoparticles were separated by adding acetone as nonsolvents and redispersed in chloroform for further use.

Characterization of the Nanoparticles. The as-prepared nanoparticles were characterized with ultraviolet–visible (UV-vis) optical absorption spectroscopy, PL emission spectroscopy, X-ray diffraction (XRD) patterns, transmission electron microscopy (TEM), X-ray photoelectron spectroscopy (XPS), and Raman spectroscopy. The measurements were carried out with UV-vis 2550 Shimadzu Spectrometer, Spex Fluoromax 4P Emission Spectrophotometer, Bruker D8 Advance X-ray Powder Diffractometer, Jeol Model JEM-2100F, Omicron (Serial No. 0571), and Horiba Jobin-Yvon Raman Triple Grating Spectrometer System (model T64000), respectively. To confirm if the MoO_3 nanoparticles was *p*-type in nature, we recorded tunneling current of an ultrathin film of the nanoparticles and their density of states with a Nanosurf Easyscan2 scanning tunneling microscope (STM) in an ambient condition. This enabled us to locate the conduction and valence band-edges of the semiconductor with respect to its Fermi energy. For STM measurements, tip voltage was applied with respect to the substrate.

Preparation of GO Dispersed Solution and a Mixed Solution of PEDOT:PSS and GO for Film Formation. The purified GO was further dried in a vacuum oven at 60 °C; the paste turned into dry graphene oxide flakes. One milligram (1 mg) of GO flakes was added to 1 mL of deionized water; the mixture was sonicated for a considerable period of time to form a dispersed solution of GO. To form a mixed solution of PEDOT:PSS and GO, 1 mL of PEDOT:PSS solution was added to a part of the dispersed solution of GO; the weight ratio of GO and PEDOT:PSS was 1:13. After a thorough sonication, the solution, which contained a mixture of PEDOT:PSS and GO, was used for film formation. Thickness of the layers of the devices was measured by forming thin films of the materials separately. To do so, a depth profile of an intentional scratch on each of the films

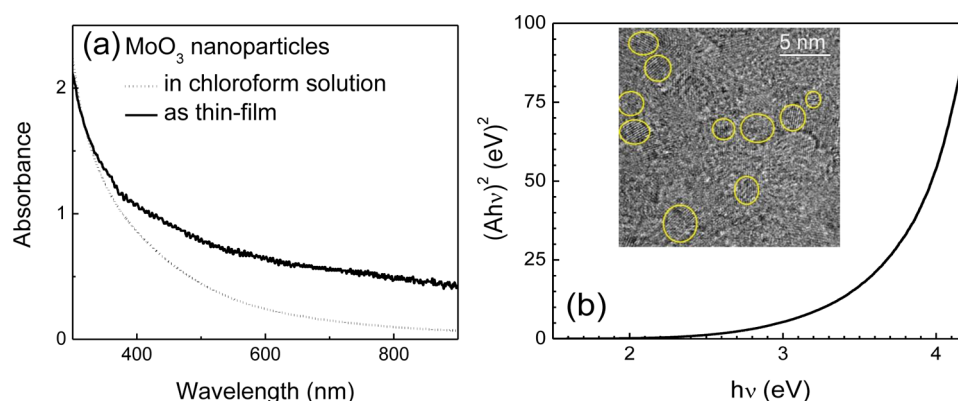


Figure 1. (a) Optical absorption spectra of MoO₃ nanoparticles in dispersed solution and in thin-film form. (b) $(A\hbar\nu)^2$ versus energy plot of the solution of nanoparticles; a TEM image of MoO₃ nanoparticles is shown in the inset of panel b.

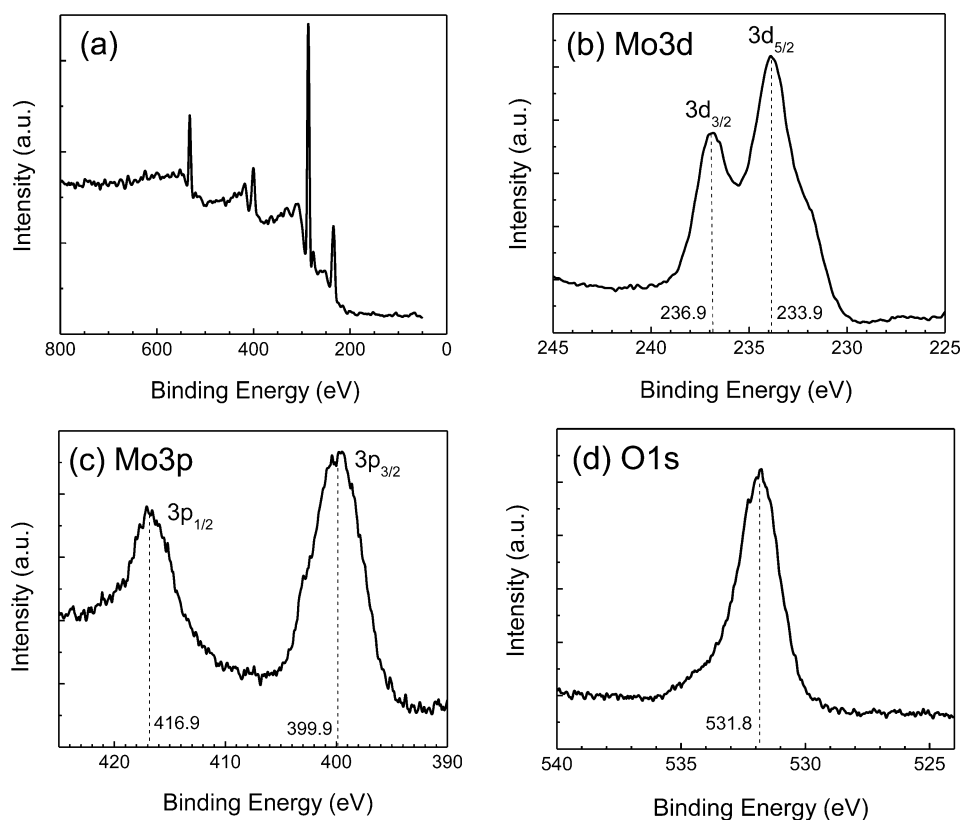


Figure 2. (a) Full-range XPS spectrum of MoO₃ nanoparticles. High-resolution XPS spectra of (b) Mo 3d, (c) Mo 3p, and (d) O 1s in small energy regions are also shown.

was imaged and recorded with an atomic force microscope (Nanosurf Easyscan2).

Device Fabrication. We have fabricated sandwiched structures with four different device configurations. They are represented as follows:

- Device #1: ITO/PEDOT:PSS/AIZS/ZnO/Al
- Device #2: ITO/PEDOT:PSS(GO)/AIZS/ZnO/Al
- Device #3: ITO/GO/AIZS/ZnO/Al
- Device #4: ITO/ZnO/AIZS/GO/MoO₃/Al

In devices #1–3, ITO was used as a positive electrode for hole injection. In device #4, which is an inverted structure, ITO acted as an electron-inject electrode.

The LEDs were fabricated on ITO-coated glass substrates having a surface resistance of 15 Ω/□. The ITO substrates were etched suitably to obtain strips 3 mm wide. The substrates were thoroughly cleaned in soap solution, methanol, acetone, and hot 2-propanol under

sonication in sequence. The ITO electrodes were treated with oxygen plasma to lower the contact resistance with the active layer. The layer of PEDOT:PSS or PEDOT:PSS(GO) was spun at 5000 rpm, followed by an annealing at 150 °C in a nitrogen environment for 15 min to remove water from the PSS shell of the PEDOT:PSS grains. To form a layer of GO, 1 mg/mL solution of the material in deionized water was spun at 1200 rpm, following the same annealing protocol. A thin film of the emitting AIZS nanocrystals was spun at 1600 rpm from 20 mg/mL chloroform solution and was annealed at 130 °C for 25 min. The layer of ZnO nanoparticles was similarly spun from 20 mg/mL ethanol solution at 2000 rpm and was annealed at 110 °C for 10 min. In the device where a layer of MoO₃ nanoparticles was deposited, the nanocrystals were spun from 15 mg/mL chloroform solution at 2000 rpm; the thin film was annealed at 130 °C for 15 min. The thin films of PEDOT:PSS or PEDOT:PSS(GO), AIZS, ZnO, and MoO₃ had thicknesses of 40, 60, 45, and 50 nm, respectively, as are being

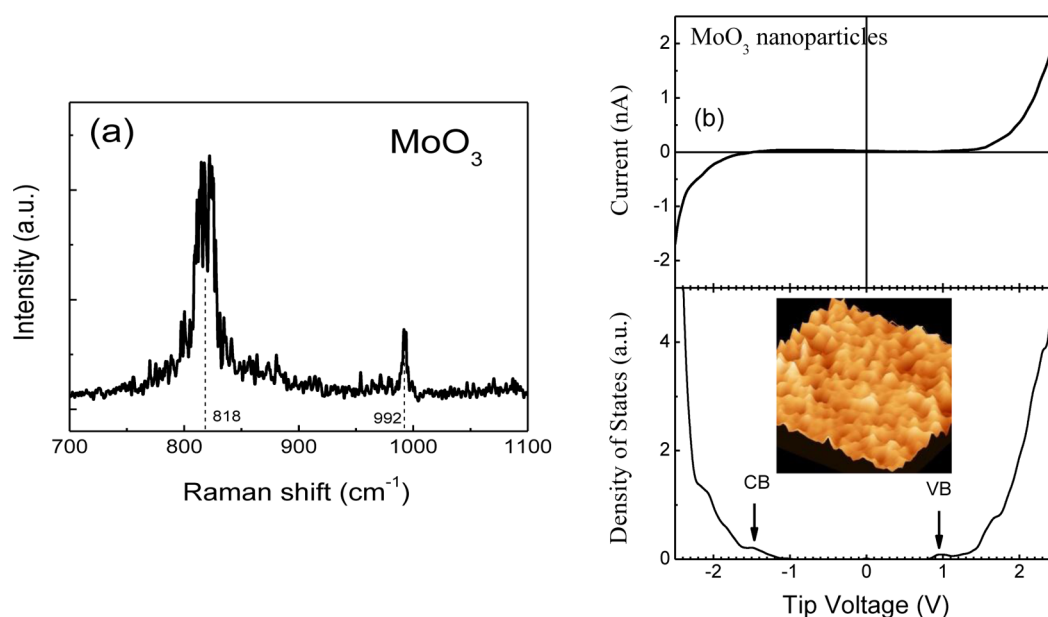


Figure 3. (a) Raman spectrum of MoO₃ nanoparticles in thin-film form. (b) Tunneling current versus tip voltage and density of states of MoO₃ showing the location of conduction band (CB) and valence band (VB) edges; inset shows a STM topography of a film (250 nm × 250 nm).

conventionally used in QDLEDs. As the top electrode for all the devices, aluminum strips 100 nm thick, orthogonal to the ITO electrodes, were thermally evaporated at a pressure of 5×10^{-6} Torr to complete the device fabrication process. The active area of each device was 9 mm².

Characterization of the Devices. The LEDs were characterized in a shielded vacuum chamber fitted with a quartz window. Current–voltage (*I*–*V*) characteristics of the devices were measured with a Keithley Dual-Channel System SourceMeter Instrument (Model 2636A). The luminous output of the devices was measured with a Konica Minolta Luminance Meter (Model LS-110). All the instruments were operated through LabVIEW software. For each of the four device architectures, we have presented characteristics from three different cells to show the degree of reproducibility of the results. The spectral response of EL emission was recorded with a Spex Fluoromax 4P Emission spectrophotometer after blocking the excitation beam.

RESULTS AND DISCUSSION

Characterization of MoO₃ Nanocrystals. The MoO₃ nanocrystals were characterized by recording optical absorption spectroscopy, TEM images, and XPS and Raman spectra. Figure 1a shows an optical absorption spectrum of MoO₃ nanoparticles dispersed in chloroform solution. A spectrum of a thin film of the oxide, as has been used in fabricating devices, is also shown in the plot. The spectra extend to the low-wavelength region. From the slope of $(A\hbar\nu)^2$ versus energy plot of the nanoparticles in dispersed solution (Figure 1b), we aimed to determine the bandgap of the oxide, which turned out to be in the range of 2.7–3.6 eV. Here, *A* is the absorbance, \hbar is Planck's constant, and ν is the frequency. From the TEM image of the nanocrystals, as shown in the inset of Figure 1b, we could determine the diameter of the nanoparticles to be between 2 and 3 nm, with a *d*-spacing of 0.22 nm.

Valence state information and elemental composition of MoO₃ nanocrystals were studied by XPS analysis. Full scan spectrum from the nanocrystals is shown in Figure 2a. The spectrum shows the presence of Mo 3d, Mo 3p, and O 1s peaks, confirming occurrence of the elements in the nanomaterial. We have also recorded high-resolution spectrum in small energy regions around each of the peaks. As can be observed in

Figure 2b, the spectrum for Mo 3d resolved into 3d_{5/2} and 3d_{3/2} peaks at 233.9 and 236.9 eV, respectively. Figure 2c similarly shows that the spectrum for Mo 3p is resolved into 3p_{3/2} and 3p_{1/2} peaks at 399.9 and 416.9 eV, respectively. These energy positions are in concurrence with the reported XPS spectrum of Mo(VI).^{20,35,36} Figure 2d shows that the spectrum corresponding to oxygen appeared at 531.8 eV, indicating the existence of the O 1s state. Our results hence imply that MoO₃ formed in the nanocrystals.

Raman spectrum also supported formation of MoO₃ exhibiting peaks at 818 and 992 cm^{−1} (Figure 3a). While the peak at 818 cm^{−1} represents the doubly coordinated oxygen–molybdenum (Mo–O–Mo) stretching vibration, the peak at 992 cm^{−1} represents stretching vibration of the metal with the terminal oxygen (Mo⁶⁺=O).³⁵ The *p*-type nature of the MoO₃ was confirmed by recording STM characteristics of a few monolayers of the nanocrystals. The STM topography of a typical film on a high-conducting (doped) silicon wafer is shown in the inset of Figure 3b. From the tunneling current versus tip voltage plot, we calculated the density of states (DOS) of MoO₃ (Figure 3b). The DOS spectrum enabled us to locate the conduction and valence band-edges of the semiconductor with the work function of the tip being aligned to the Fermi energy of MoO₃. Since the bias was applied with respect to the substrate, the tip at a positive voltage withdraws electrons from the nanoparticles; the peaks in the DOS spectrum hence denote the valence bands of the nanoparticles. Similarly, the peaks at negative voltages, at which electrons could be injected from the tip, provide the location of the conduction bands. Here, under an equilibrium condition, the zero voltage matches the Fermi energy of the semiconductor. The results show that the transport gap of the nanoparticles was 2.42 eV, which is expectedly slightly lower than the optical gap. The results more importantly show that the Fermi energy was closer to the valence band-edge, depicting the *p*-type nature of MoO₃ nanoparticles.

Characterization of GO. The graphene oxide flakes were also characterized in a similar manner. The optical absorption

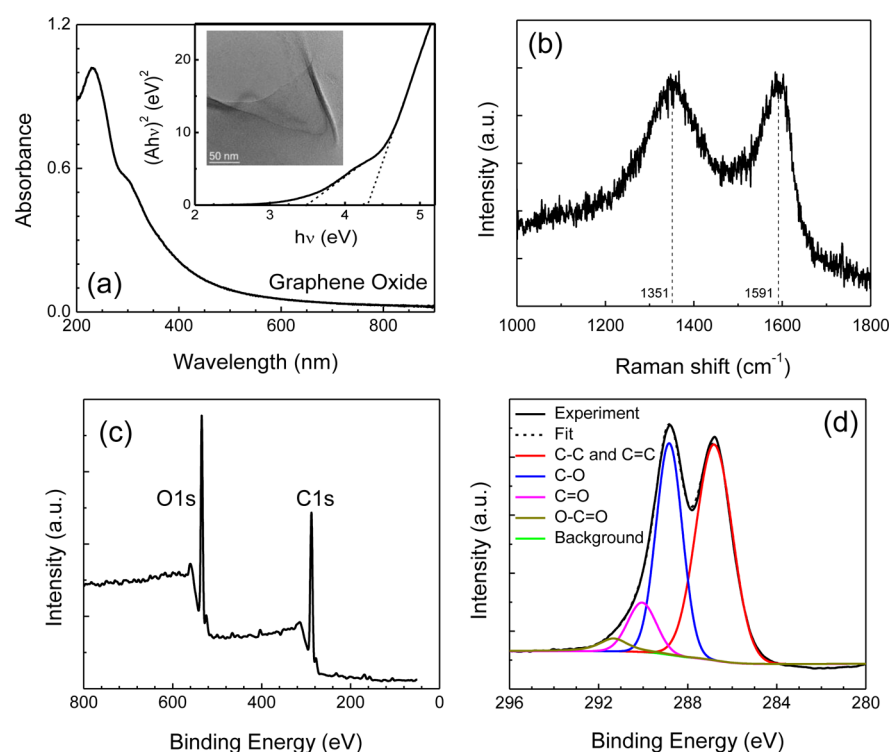


Figure 4. (a) Optical absorption spectrum of GO in dispersed solution along with a TEM image of the GO. $(A\hbar\nu)^2$ versus energy plot of the solution of GO is shown in the inset. (b) Raman spectrum of the carbon allotrope thin film. (c) Full-range and (d) high-resolution XPS spectra of GO. In panel d, deconvoluted four peaks of the spectrum are shown.

and Raman spectra, as shown in Figures 4a and 4b, respectively, match with reported results.^{37–39} Absorption spectrum showed a peak at 230 nm along with a shoulder at 303 nm, which correspond to $\pi \rightarrow \pi^*$ and $n \rightarrow \pi^*$ transitions of C=O. Band gap ranges between 3.5 and 4.25 eV as per the $(A\hbar\nu)^2$ versus energy plot (inset of Figure 4a).³⁹ Raman spectrum of the flakes yielded two peaks at 1351 and 1591 cm^{-1} . The sharp peak at 1591 cm^{-1} is the G-peak corresponding to the in-plane stretching vibration of graphite lattice; the peak at 1351 cm^{-1} is the D-peak arising out of small-sized graphitic domains. In the TEM image of GO, as shown in the inset of Figure 4a, an ordered graphene sheet is clearly visible.

In Figures 4c and 4d, we display XPS spectra of GO in the full scale and for the C 1s region. The peak in the C 1s region that matches with the reported results,^{38–40} can be deconvoluted into four peaks with the major one being at 286.8 eV, which represents C–C and C=C bonds of carbon atoms in a conjugated honeycomb lattice. The other two peaks at 288.8 and 290.1 eV represent different C–O bonding configurations of oxygenated carbon. A fourth low-intensity peak appearing at 291.3 eV and representing O–C=O bonds are also consistent with the reported results with a slight shift in energy.

Characterization of AIZS Nanoparticles. Optical absorption and PL spectra of AIZS nanoparticles dispersed in chloroform solution are shown in Figure 5. Bandgap of the nanoparticles can be controlled during the growth process by varying the molar ratio of silver and zinc ($M_{[\text{Ag}]} / M_{[\text{Zn}]}$).¹⁶ In this work, we have selected that ratio to be 0.25 at which the nanoparticles emit emissions in the yellow region. With such a ratio, the intensity of PL emission reaches a maximum; the PL band at 568 nm had a quantum yield of 37%. The full width at half-maximum (fwhm) of the PL emission was ~ 126 nm. In

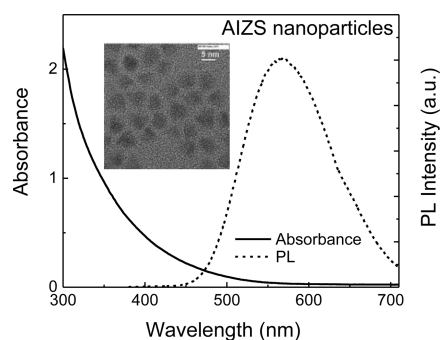


Figure 5. Optical absorption and photoluminescence (PL) spectra of AIZS nanoparticles in dispersed solution. A TEM image of the nanoparticles is shown in the inset of the figure.

chalcopyrite-type I–III–VI₂ ternary semiconductor particles, such as CuInS₂ (CIS) and AgInS₂ (AIS), a broad emission peak having a fwhm larger than 100 nm is generally observed and has been assigned to radiative transitions in donor–acceptor levels and/or emission from trap sites.⁴¹ We hence infer that the PL emission in AIZS nanoparticles originates from donor–acceptor recombination of the carriers in the nanoparticles. A TEM image of the nanoparticles is shown in the inset of the figure. The particles can be found to be monodispersed with a diameter of ~ 5 nm.

Characterization of ZnO Nanoparticles. The ZnO nanoparticles were characterized through usual methods, such as optical absorption spectroscopy, TEM images, and XRD patterns (Figure 6). The characteristics match the reported results confirming formation of ZnO nanoparticles. The lattice planes in diffraction patterns as shown in Figure 6b confirmed

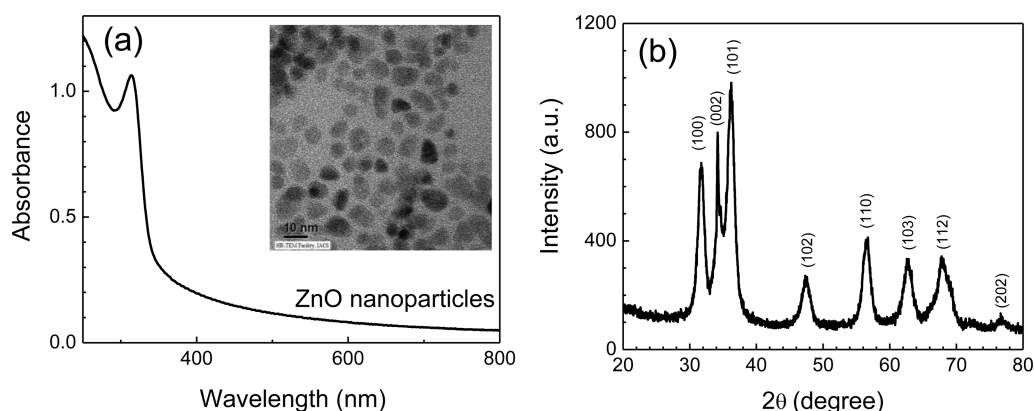


Figure 6. (a) Optical absorption spectrum and (b) XRD patterns of ZnO nanoparticles. A TEM image of the nanoparticles is shown in the inset of panel a.

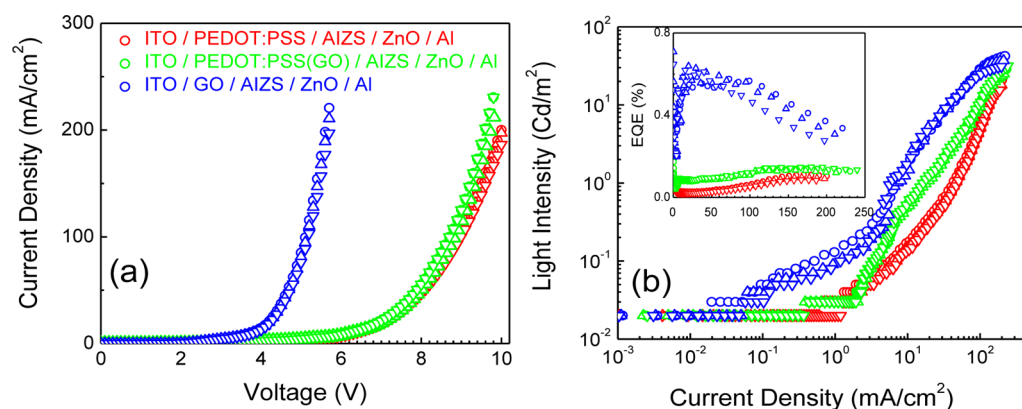


Figure 7. (a) Current–voltage and (b) EL intensity versus current plots of QDLEDs. Device architecture is shown as legends. For each of the device architectures, characteristics from three indistinguishable cells for each device architecture are shown using different symbols. In the inset of panel b, EQE% versus current density plots of these devices are shown.

formation of the wurtzite phase of ZnO, when compared with JCPDS File Card No. 36-1451.

Characterization of QDLEDs. We have recorded current–voltage and luminous intensity versus current density characteristics of the QDLEDs. In Figure 7, we show plots for the three devices, namely devices #1–3, that have different hole-inject layers, namely PEDOT:PSS, PEDOT:PSS(GO), and GO. While a layer of AIZS quantum dots was the active emitting material in all the devices, the ZnO-layer acted as an electron-transport layer in these three devices. It may be stated that the device current in QDLEDs is generally dominated by electrons. When we compare characteristics of devices #1 and #2, we observe that the device #2 with PEDOT:PSS(GO) yielded a higher current at a voltage compared to device #1 that had only PEDOT:PSS as the hole-inject layer. This is due to the fact that with an addition of GO in PEDOT:PSS solution, the GO replace the insulating PSS chains from the PEDOT thereby enhancing the conductivity, compared to the PEDOT:PSS-only thin film.⁴² Also, the addition of GO makes the PEDOT more quinoidal and thus more conductive.⁴² In device #3, where we replaced the PEDOT:PSS with GO, the device current was the highest, because of the thinness of GO as the hole-inject layer. To eliminate the effect of thickness of the carrier inject or transport layers, we have plotted EL intensity versus current density plots of the devices (Figure 7b). In device #3, the EL intensity at any device current was the highest, compared to the other two devices. This is due to the electron-blocking nature

of GO that encourages the formation of excitons in the emitting layer. While PEDOT:PSS and GO both act as hole-inject materials, PEDOT:PSS cannot block electrons to reach the ITO. The wide-bandgap GO in devices #2 and #3, on the other hand, acts both as a hole-transport layer and an electron-blocking layer. The latter property of GO facilitates exciton generation in the emitting layer and thereby increased EL output. The introduction of GO could moreover make the device free from the polymer, which is detrimental to the stability issues of polymer-based devices.

With the advantages of GO as a hole-transport layer, we observe that device #3 has a lower turn-on current, compared to the other two devices (Figure 7b). External quantum efficiency (EQE%) spectrum of the GO-based device was also favorable. The inset of Figure 7b shows that the EQE% at any device current was much higher in device #3, compared to the other two device architectures.

Inverted QDLEDs with MoO₃ Nanoparticles as Hole-Inject Layer. With the success of GO as a hole-transport layer, we noted a further scope of improvement. It may be advantageous to form an inverted device architecture with ITO as a cathode. With ZnO and GO continuing to act as an electron- and hole-transport material, respectively, there is now a need to introduce a hole-inject layer of MoO₃ nanoparticles, since a low work function of the anode (aluminum) may not be suitable to inject holes in the GO. In such an inverted device architecture (ITO/ZnO/AIZS/GO/MoO₃/Al) as shown in the

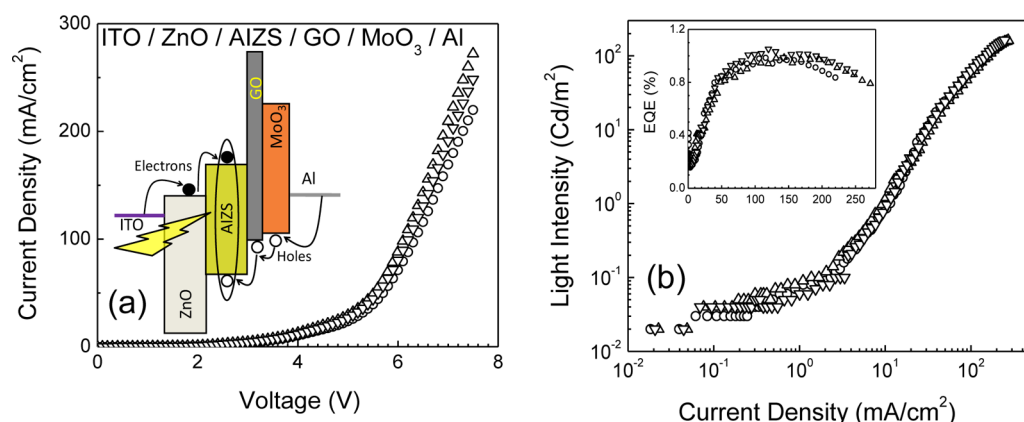


Figure 8. (a) Current–voltage and (b) EL intensity versus current plots of QDLED of device #4, that is, ITO/ZnO/AIZS/GO/MoO₃/Al. A schematic representation of the device is shown in the inset of panel a. In the inset of panel b, a plot of EQE% versus current density of the devices are shown. Here also, characteristics from three cells are shown, using different symbols.

inset of Figure 8a, the low bandgap MoO₃ nanoparticles would not block the exit of EL emission; the ZnO which is transparent in the visible region of solar spectrum, is an ideal material to put on the semitransparent electrode. A balance in charge injection is achieved due to the introduction of MoO₃ nanoparticles as a hole-inject layer and also a higher barrier-height for electrons due to the ZnO layer. Moreover, the GO and MoO₃ layers would block flow of electrons to the Al-electrode and thereby reduce device current in the QDLEDs; moreover, the ZnO layer would block flow of holes to the ITO electrode. These two events hence facilitate formation of excitons in AIZS nanoparticles that finally yield EL emission. In Figure 8, we plot current–voltage and luminance–current characteristics and EQE spectrum of the inverted devices. We observe that as compared to devices #1–3, the inverted structure (device #4) yielded a lower current at any voltage primarily due to the barrier (for electrons) introduced by the ZnO layer in the inverted structure. Despite a lower device current, a much-higher light output was observed. A balance in charge injection, a facile hole-injection upon introduction of hole-inject layer (MoO₃ nanoparticles), and the presence of carrier-blocking layers must have facilitated the formation of excitons in the layer of AIZS nanoparticles. The EQE% also was much higher in this structure, as shown in the inset of Figure 8b. The peak in the EQE (%) versus current density plot that appears when exciton formation was optimized was flat (as compared to devices #1–3) implying optimum device performance in a wider range of device current.

Electroluminescence Spectra of QDLEDs. We recorded EL spectrum of the devices to verify if the emission appeared solely from AIZS nanoparticles (see Figure 9). For comparison, we have added PL spectrum of (thin films of) the nanoparticles. The wavelength of the peak in the EL emission is ~8 nm higher than that of the PL one of AIZS nanoparticles. The nature of the EL and PL spectra match well, implying that the excitons formed and decayed radiatively in AIZS nanoparticles exemplifying fabrication of QDLEDs with oxides as carrier inject and transport layers.

CONCLUSIONS

In conclusion, we have fabricated quantum dot light-emitting diodes (QDLEDs) based on a layer of AIZS nanoparticles as the emitting material. In addition, we have used oxides, namely graphene oxide and zinc oxide as hole- and electron-transport

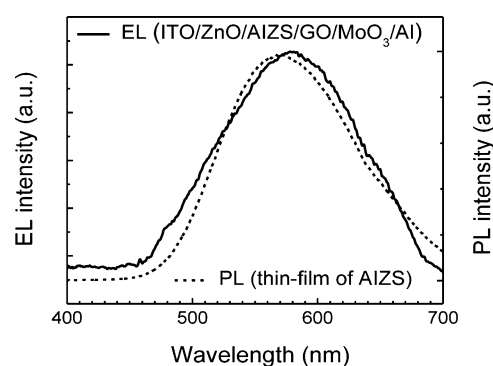


Figure 9. EL spectrum of a QDLED based on an active layer of AIZS nanocrystals in inverted device structure at an applied voltage of 6.0 V. PL spectrum of a thin film of AIZS nanoparticles is also shown in the figure.

layer, respectively. To bring the transparent zinc oxide next to the semitransparent electrode (ITO) so that exit of electroluminescence is not blocked, we formed an inverted structure, ITO/ZnO/AIZS/GO/MoO₃/Al, where ITO and aluminum acted as electron- and hole-inject electrode, respectively. In such a structure, we introduced a layer of the nanoparticles of MoO₃ as a hole-inject layer to lower the barrier height for hole injection for improved device performance. Here, GO and MoO₃ layers blocked flow of electrons through the device and thereby reduce device current in the QDLEDs; the ZnO layer moreover blocked flow of holes to the ITO electrode. These two events hence forced the carriers to form excitons in the AIZS layer that finally yielded EL emission. Such an inverted structure yielded a higher EL emission that matched well with the PL spectrum of AIZS nanoparticles implying that excitons were formed in the quaternary nanocrystals and decayed radiatively. The results hence demonstrate solution-processed QDLEDs with the emitting nanocrystals being based on nontoxic and Earth-abundant elements and oxides as carrier inject and transport layers.

AUTHOR INFORMATION

Corresponding Author

*Tel.: +91-33-24734971. Fax: +91-33-24732805. E-mail: sspajp@iacs.res.in.

Notes

The authors declare no competing financial interest.

ACKNOWLEDGMENTS

The authors acknowledge thank Tanmoy Maji and Prof. Tarun K. Mandal of Polymer Science Unit, Indian Association for the Cultivation of Science for providing graphene oxides. The work of SB was funded by CSIR–Junior Research Fellowship No. 09/080(0692)/2010-EMR-I (Roll No. 507693). The authors acknowledge funding from DST Nano Mission projects.

REFERENCES

- Schlamp, M. C.; Peng, X. G.; Alivisatos, A. P. Improved Efficiencies in Light Emitting Diodes Made with CdSe(CdS) Core/Shell Type Nanocrystals and a Semiconducting Polymer. *J. Appl. Phys.* **1997**, *82*, 5837–5842.
- Könenkamp, R.; Word, R. C.; Godinez, M. Ultraviolet Electroluminescence from ZnO/Polymer Heterojunction Light-Emitting Diodes. *Nano Lett.* **2005**, *5*, 2005–2008.
- Rizzo, A.; Li, Y. Q.; Kuder, S.; Della Sala, F.; Zanella, M.; Parak, W. J.; Cingolani, R.; Manna, L.; Gigli, G. Blue Light-Emitting Diodes Based on Fluorescent CdSe/ZnS Nanocrystals. *Appl. Phys. Lett.* **2007**, *90*, 051106.
- Rath, A. K.; Bhaumik, S.; Pal, A. J. Mn-doped Nanocrystals in Light-Emitting Diodes: Energy-Transfer to Obtain Electroluminescence from Quantum Dots. *Appl. Phys. Lett.* **2010**, *97*, 113502.
- Bhaumik, S.; Ghosh, B.; Pal, A. J. Color Tunable Light-Emitting Diodes Based on Copper Doped Semiconducting Nanocrystals. *Appl. Phys. Lett.* **2011**, *99*, 083106.
- Madan, S.; Kumar, J.; Madhwal, D.; Singh, I.; Bhatnagar, P. K.; Mathur, P. C. Color Tuning and Improved Performance of Poly[2-Methoxy-5-(2'-Ethyl-Hexyloxy)-1,4-Phenylenevinylene]-based Polymer Light Emitting Diode using Cadmium Selenide/Zinc Sulphide Core Shell Uncapped Quantum Dots as Dopants. *J. Nanophotonics* **2011**, *5*, 053518.
- Kwak, J.; Bae, W. K.; Lee, D.; Park, I.; Lim, J.; Park, M.; Cho, H.; Woo, H.; Yoon, D. Y.; Char, K.; Lee, S.; Lee, C. Bright and Efficient Full-Color Colloidal Quantum Dot Light-Emitting Diodes Using an Inverted Device Structure. *Nano Lett.* **2012**, *12*, 2362–2366.
- Pal, B. N.; Ghosh, Y.; Brovelli, S.; Laocharoensuk, R.; Klimov, V. I.; Hollingsworth, J. A.; Htoon, H. 'Giant' CdSe/CdS Core/Shell Nanocrystal Quantum Dots As Efficient Electroluminescent Materials: Strong Influence of Shell Thickness on Light-Emitting Diode Performance. *Nano Lett.* **2012**, *12*, 331–336.
- Son, D. I.; Kwon, B. W.; Park, D. H.; Seo, W.-S.; Yi, Y.; Angadi, B.; Lee, C.-L.; Choi, W. K. Emissive ZnO-Graphene Quantum Dots for White-Light-Emitting Diodes. *Nat. Nanotechnol.* **2012**, *7*, 465–471.
- Sun, L.; Choi, J. J.; Stachnik, D.; Bartnik, A. C.; Hyun, B.-R.; Malliaras, G. G.; Hanrath, T.; Wise, F. W. Bright Infrared Quantum-Dot Light-Emitting Diodes through Inter-Dot Spacing Control. *Nat. Nanotechnol.* **2012**, *7*, 369–373.
- Bae, W. K.; Kwak, J.; Lim, J.; Lee, D.; Nam, M. K.; Char, K.; Lee, C.; Lee, S. Multicolored Light-Emitting Diodes Based on All-Quantum-Dot Multilayer Films Using Layer-by-Layer Assembly Method. *Nano Lett.* **2010**, *10*, 2368–2373.
- Qian, L.; Zheng, Y.; Xue, J. G.; Holloway, P. H. Stable and Efficient Quantum-Dot Light-Emitting Diodes Based on Solution-Processed Multilayer Structures. *Nat. Photonics* **2011**, *5*, 543–548.
- Yang, X.; Ma, Y.; Mutlugun, E.; Zhao, Y.; Leck, K. S.; Tan, S. T.; Demir, H. V.; Zhang, Q.; Du, H.; Sun, X. W. Stable, Efficient, and All-Solution-Processed Quantum Dot Light-Emitting Diodes with Double-Sided Metal Oxide Nanoparticle Charge Transport Layers. *ACS Appl. Mater. Interfaces* **2014**, *6*, 495–499.
- Chen, B. K.; Zhong, H. Z.; Zhang, W. Q.; Tan, Z. A.; Li, Y. F.; Yu, C. R.; Zhai, T. Y.; Bando, Y. S.; Yang, S. Y.; Zou, B. S. Highly Emissive and Color-Tunable CuInS₂-Based Colloidal Semiconductor Nanocrystals: Off-Stoichiometry Effects and Improved Electroluminescence Performance. *Adv. Funct. Mater.* **2012**, *22*, 2081–2088.
- Tan, Z.; Zhang, Y.; Xie, C.; Su, H.; Liu, J.; Zhang, C.; Dellas, N.; Mohny, S. E.; Wang, Y.; Wang, J.; Xu, J. Near-Band-Edge Electroluminescence from Heavy-Metal-Free Colloidal Quantum Dots. *Adv. Mater.* **2011**, *23*, 3553–3558.
- Bhaumik, S.; Guchhait, A.; Pal, A. J. Light-Emitting Diodes Based on Nontoxic Zinc-Alloyed Silver–Indium-Sulfide (AIZS) Nanocrystals. *Physica E* **2014**, *58*, 124–129.
- Bhargava, R. N.; Gallagher, D.; Hong, X.; Nurmikko, A. Optical-Properties of Manganese-Doped Nanocrystals of ZnS. *Phys. Rev. Lett.* **1994**, *72*, 416–419.
- Xie, R. G.; Peng, X. G. Synthesis of Cu-Doped InP Nanocrystals (*d*-dots) with ZnSe Diffusion Barrier as Efficient and Color-Tunable NIR Emitters. *J. Am. Chem. Soc.* **2009**, *131*, 10645–10651.
- Lee, H.; Kang, C.-M.; Park, M.; Kwak, J.; Lee, C. Improved Efficiency of Inverted Organic Light-Emitting Diodes Using Tin Dioxide Nanoparticles as an Electron Injection Layer. *ACS Appl. Mater. Interfaces* **2013**, *5*, 1977–1981.
- Fu, Q.; Chen, J.; Shi, C.; Ma, D. Room-Temperature Sol-Gel Derived Molybdenum Oxide Thin Films for Efficient and Stable Solution-Processed Organic Light-Emitting Diodes. *ACS Appl. Mater. Interfaces* **2013**, *5*, 6024–6029.
- Kim, H.-M.; Youn, J.-H.; Seo, G.-J.; Jang, J. Inverted Quantum-Dot Light-Emitting Diodes with Solution-Processed Aluminium-Zinc Oxide as a Cathode Buffer. *J. Mater. Chem. C* **2013**, *1*, 1567–1573.
- Mashford, B. S.; Nguyen, T. L.; Wilson, G. J.; Mulvaney, P. All-Inorganic Quantum-Dot Light-Emitting Devices Formed via Low-Cost, Wet-Chemical Processing. *J. Mater. Chem.* **2010**, *20*, 167–172.
- Caruge, J. M.; Halpert, J. E.; Wood, V.; Bulovic, V.; Bawendi, M. G. Colloidal Quantum-Dot Light-Emitting Diodes with Metal-Oxide Charge Transport Layers. *Nat. Photonics* **2008**, *2*, 247–250.
- He, S.; Li, S.; Wang, F.; Wang, A. Y.; Lin, J.; Tan, Z. A. Efficient Quantum Dot Light-Emitting Diodes with Solution-Processable Molybdenum Oxide as the Anode Buffer Layer. *Nanotechnology* **2013**, *24*, 175201.
- Cho, K.-S.; Lee, E. K.; Joo, W.-J.; Jang, E.; Kim, T.-H.; Lee, S. J.; Kwon, S.-J.; Han, J. Y.; Kim, B.-K.; Choi, B. L.; Kim, J. M. High-Performance Crosslinked Colloidal Quantum-Dot Light-Emitting Diodes. *Nat. Photonics* **2009**, *3*, 341–345.
- Lee, B. R.; Kim, J.-W.; Kang, D.; Lee, D. W.; Ko, S.-J.; Lee, H. J.; Lee, C.-L.; Kim, J. Y.; Shin, H. S.; Song, M. H. Highly Efficient Polymer Light-Emitting Diodes Using Graphene Oxide as a Hole Transport Layer. *ACS Nano* **2012**, *6*, 2984–2991.
- Shi, S.; Sadhu, V.; Moubah, R.; Schmerber, G.; Bao, Q.; Silva, S. R. P. Solution-Processable Graphene Oxide as an Efficient Hole Injection Layer for High Luminance Organic Light-Emitting Diodes. *J. Mater. Chem. C* **2013**, *1*, 1708–1712.
- Stubhan, T.; Ameri, T.; Salinas, M.; Krantz, J.; Machui, F.; Halik, M.; Brabec, C. J. High Shunt Resistance in Polymer Solar Cells Comprising a MoO₃ Hole Extraction Layer Processed From Nanoparticle Suspension. *Appl. Phys. Lett.* **2011**, *98*, 253308.
- Huang, J. H.; Huang, T. Y.; Wei, H. Y.; Ho, K. C.; Chu, C. W. Wet-Milled Transition Metal Oxide Nanoparticles as Buffer Layers for Bulk Heterojunction Solar Cells. *RSC Adv.* **2012**, *2*, 7487–7491.
- Mashford, B. S.; Stevenson, M.; Popovic, Z.; Hamilton, C.; Zhou, Z.; Breen, C.; Steckel, J.; Bulovic, V.; Bawendi, M.; Coe-Sullivan, S.; Kazlas, P. T. High-Efficiency Quantum-Dot Light-Emitting Devices with Enhanced Charge Injection. *Nat. Photonics* **2013**, *7*, 407–412.
- Bae, W. K.; Park, Y.-S.; Lim, J.; Lee, D.; Padilha, L. A.; McDaniel, H.; Robel, I.; Lee, C.; Pietryga, J. M.; Klimov, V. I. Controlling the Influence of Auger Recombination on the Performance of Quantum-Dot Light-Emitting Diodes. *Nat. Commun.* **2013**, *4*, 2661.
- Manna, G.; Jana, S.; Bose, R.; Pradhan, N. Mn-Doped Multinary CIZS and AIZS Nanocrystals. *J. Phys. Chem. Lett.* **2012**, *3*, 2528–2534.
- Schwartz, D. A.; Norberg, N. S.; Nguyen, Q. P.; Parker, J. M.; Gamelin, D. R. Magnetic Quantum Dots: Synthesis, Spectroscopy, and Magnetism of Co²⁺- and Ni²⁺-Doped ZnO Nanocrystals. *J. Am. Chem. Soc.* **2003**, *125*, 13205–13218.

- (34) Hummers, W. S.; Offeman, R. E. Preparation of Graphitic Oxide. *J. Am. Chem. Soc.* **1958**, *80*, 1339–1339.
- (35) Rajagopal, S.; Nataraj, D.; Khyzhun, O. Y.; Djaoued, Y.; Robichaud, J.; Senthil, K.; Mangalaraj, D. Systematic Synthesis and Analysis of Change in Morphology, Electronic Structure and Photoluminescence Properties of Pyrazine Intercalated MoO₃ Hybrid Nanostructures. *CrystEngComm* **2011**, *13*, 2358–2368.
- (36) Scanlon, D. O.; Watson, G. W.; Payne, D. J.; Atkinson, G. R.; Egde, R. G.; Law, D. S. L. Theoretical and Experimental Study of the Electronic Structures of MoO₃ and MoO₂. *J. Phys. Chem. C* **2010**, *114*, 4636–4645.
- (37) Eda, G.; Chhowalla, M. Chemically Derived Graphene Oxide: Towards Large-Area Thin-Film Electronics and Optoelectronics. *Adv. Mater.* **2010**, *22*, 2392–2415.
- (38) Mei, X.; Ouyang, J. Ultrasonication-Assisted Ultrafast Reduction of Graphene Oxide by Zinc Powder at Room Temperature. *Carbon* **2011**, *49*, 5389–5397.
- (39) Hsu, H.-C.; Shown, I.; Wei, H.-Y.; Chang, Y.-C.; Du, H.-Y.; Lin, Y.-G.; Tseng, C.-A.; Wang, C.-H.; Chen, L.-C.; Lin, Y.-C.; Chen, K.-H. Graphene Oxide as a Promising Photocatalyst for CO₂ to Methanol Conversion. *Nanoscale* **2013**, *5*, 262–268.
- (40) Shang, J.; Ma, L.; Li, J.; Ai, W.; Yu, T.; Gurzadyan, G. G. The Origin of Fluorescence from Graphene Oxide. *Sci. Rep.* **2012**, *2*, 792.
- (41) Torimoto, T.; Adachi, T.; Okazaki, K.; Sakuraoka, M.; Shibayama, T.; Ohtani, B.; Kudo, A.; Kuwabata, S. Facile Synthesis of ZnS–AgInS₂ Solid Solution Nanoparticles for a Color-Adjustable Luminophore. *J. Am. Chem. Soc.* **2007**, *129*, 12388–12389.
- (42) Tung, V. C.; Kim, J.; Cote, L. J.; Huang, J. X. Sticky Interconnect for Solution-Processed Tandem Solar Cells. *J. Am. Chem. Soc.* **2011**, *133*, 9262–9265.